MATERIALS CHEMISTRY FRONTIERS

CHINESE CHEMICAL SOCIETY

ROYAL SOCIETY OF CHEMISTRY

RESEARCH ARTICLE

View Article Online
View Journal | View Issue

Cite this: *Mater. Chem. Front.*, 2023, 7, 2661

Viologen linker as a strong electron-transfer mediator in the covalent organic framework to enhance electrocatalytic CO_2 reduction†

Xin Zhang,[ab] Yin-Zong Yuan,[ab] Hong-Fang Li,*[b] Qiu-Jin Wu,[bc] Hong-Jing Zhu,[bc] Yu-Liang Dong,[ab] Qiao Wu,[bc] Yuan-Biao Huang *[bc] and Rong Cao *[bcd]

Received 28th February 2023,
Accepted 5th April 2023

DOI: 10.1039/d3qm00218g

rsc.li/frontiers-materials

Covalent organic frameworks (COFs) are promising candidates for the CO_2 electroreduction reaction (CO_2RR) due to their advantages of tunable structures, abundant active sites, and strong CO_2 adsorption enrichment. However, the poor conductivities of the traditional COFs usually result in a low current density in the CO_2RR and limits their use in industrial applications. Herein, viologen units as strong electron-transfer mediators (ETMs) were inserted into the backbones of Co-porphyrin-based COF (Por(Co)-Vg-COF) nanosheets to enhance the electronic conductivity and improve the CO_2RR activity. The obtained Por(Co)-Vg-COF displayed a good conductivity of 3.7×10^{-7} S m^{-1} and thus exhibited a very high selectivity towards CO production (>98%) in a wide range of applied potentials from −0.6 V to −0.9 V *versus* the reversible hydrogen electrode (RHE) in neutral aqueous solution, which surpassed all the conventional COF electrocatalysts. Moreover, Por(Co)-Vg-COF was employed as the first COF electrode in an acidic/alkaline system, and achieved a high FE_{CO} of up to 91% at −0.9 V *versus* RHE in acidic electrolyte and a current density of 251 mA cm^{-2} at −1.3 V *versus* RHE in 1 M KOH aqueous electrolyte. This work provides a facile strategy to enhance the CO_2RR performance by improving the electronic conductivity of porous framework materials *via* the introduction of an ETM in their backbone.

Introduction

Clean and sustainable energy-conversion technologies are highly demanded due to the environmental and energy problems caused by large emissions of the greenhouse gas carbon dioxide (CO_2) from conventional fossil fuel-based technologies.[1] Among the clean technologies, the electrocatalytic reduction of CO_2 for value-added products using clean electric energy stands out as a particularly attractive and promising solution to reduce carbon emissions.[2–15] To date, many Au-, Ag-, and Cu-based nanostructured materials, metal–organic frameworks, and single-atom catalysts have been developed to apply in the CO_2 electroreduction reaction (CO_2RR).[16–22] However, the CO_2RR generally faces challenges in achieving high selectivity and a high current density due to the intrinsic thermodynamic stability of CO_2 and the competitive hydrogen evolution reaction (HER), hindering its practical application. Therefore, the development of highly efficient electrode materials that can overcome these problems is desirable.

Covalent organic frameworks (COFs) linked by organic building blocks with strong covalent bonds are regarded as promising candidates for the CO_2RR due to their robust frameworks, tuneable functional groups and active sites, and strong CO_2 adsorption enrichment ability.[23–31] The enriched CO_2 can easily diffuse to the exposed abundant active sites in porous COFs *via* channels. Thus, some metal porphyrin and metal phthalocyanine-based COFs have been synthesized and applied to the CO_2RR to produce CO.[1,27] However, the poor conductivity of the COFs is one of the most challenging issues still to overcome, limiting the current density and the efficiency of the energy conversion in the CO_2RR. Therefore, in order to generate high current densities, it is highly desirable to create conductive 2D COFs with efficient electron-transfer abilities for the CO_2RR. In addition, most of the COF electrocatalysts reported to date have been constructed by metastable imine bonds, which means they can be used only in H-type cells with neutral electrolytes and thus cannot afford large current densities (up to 100 mA cm^{-2}) due to the limited CO_2 concentration in neutral aqueous solutions (0.034 mol L^{-1}).[2,18,23,27] In contrast,

[a] College of Chemistry, Fuzhou University, Fuzhou, 350108, China
[b] State Key Laboratory of Structural Chemistry, Fujian Institute of Research on the Structure of Matter, Chinese Academy of Sciences, Fuzhou, 350002, Fujian, China. E-mail: hongfangli@fjirsm.ac.cn, ybhuang@fjirsm.ac.cn, rcao@fjirsm.ac.cn
[c] University of Chinese Academy of Science, Beijing 100049, China
[d] Fujian Science & Technology Innovation Laboratory for Optoelectronic Information of China, Fuzhou, 350108, Fujian, China

† Electronic supplementary information (ESI) available. See DOI: https://doi.org/10.1039/d3qm00218g

when the CO_2RR[29] is operated in a flow cell with a gas-diffusion electrode in acidic/alkaline aqueous electrolyte, it can effectively tackle the above challenges through the faster CO_2 diffusion to the catalyst surface.[33–45] However, the majority of COFs with an imine bond connected usually show poor stability in acidic/alkaline systems. Thus, it is highly desirable to construct ultra-stable COFs in acidic/alkaline aqueous solutions for the CO_2RR with an appropriate industrial-current level density to meet the needs of commercial applications.

To address the above-mentioned problems, we turned our attention to the introduction of an electron-transport mediator (ETM) into chemically stable COFs to increase the electron-transfer ability and enhance the CO_2RR in alkaline and acidic conditions. It is well known that viologens are a unique class of ETM molecules, which can undergo two- or one-electron reduction in steps.[46–48] Dicationic 4,4′-bipyridinium core (Vg^{2+}) is reversibly reducible to the corresponding radical cationic intermediate (Vg^{2+}) or to neutral (Vg^0).[49] Such redox properties have been used to enhance electrocatalysis by improving the charge-transfer ability when combined with electron-deficient molecules.[48,50–52] On the other hand, cobalt porphyrin is also considered to be an active site for CO_2RR towards the production of CO.[1,2,23,27] Moreover, cobalt porphyrin molecules are excellent electron acceptors or electron-transfer carriers because of their conjugated electron system. So, introducing viologens into the backbones of cobalt porphyrin-based COFs would be an effective strategy to improve the electronic conductivity and ultimately enhance the energy-conversion efficiency of the CO_2RR.[46,53–60] In addition, compared with most the COFs linked by imine bonds, the C–N bond is more stable in harsh conditions, which could make the COF materials constructed by C–N bonds applicable in acidic or alkaline electrolytes and thus improve the CO_2RR activity.

Herein, we introduced viologen building blocks into a C–N bond-connected robust conductive Co-porphyrin-based COF (Por(Co)-Vg-COF) to enhance the CO_2RR performance (Fig. 1(a)). The viologen groups served as ETMs to transfer the abundant electrons to the adjacent Co-porphyrin site in the Por(Co)-Vg-COF, and thus a highly efficient electrocatalytic porous material system was constructed for the CO_2RR. The obtained Por(Co)-Vg-COF displayed a one order of magnitude higher electron-conduction value (3.7×10^{-7} S m^{-1}) than that of the traditional COF-366-Co (2.08×10^{-8} S m^{-1}). Thus, the Por(Co)-Vg-COF nanosheets exhibited high CO selectivity with 98.5% Faraday efficiency at −0.6 V *versus* the reversible hydrogen electrode (RHE, all the potentials quoted in this paper are with reference to the RHE) tested using the H-cell in $KHCO_3$ electrolyte. Moreover, the robust Por(Co)-Vg-COF also showed excellent CO_2RR performance in an acidic/alkaline system. It showed excellent CO selectivity above 90% in the wider potential range of −1.2 to −1.5 V and the CO

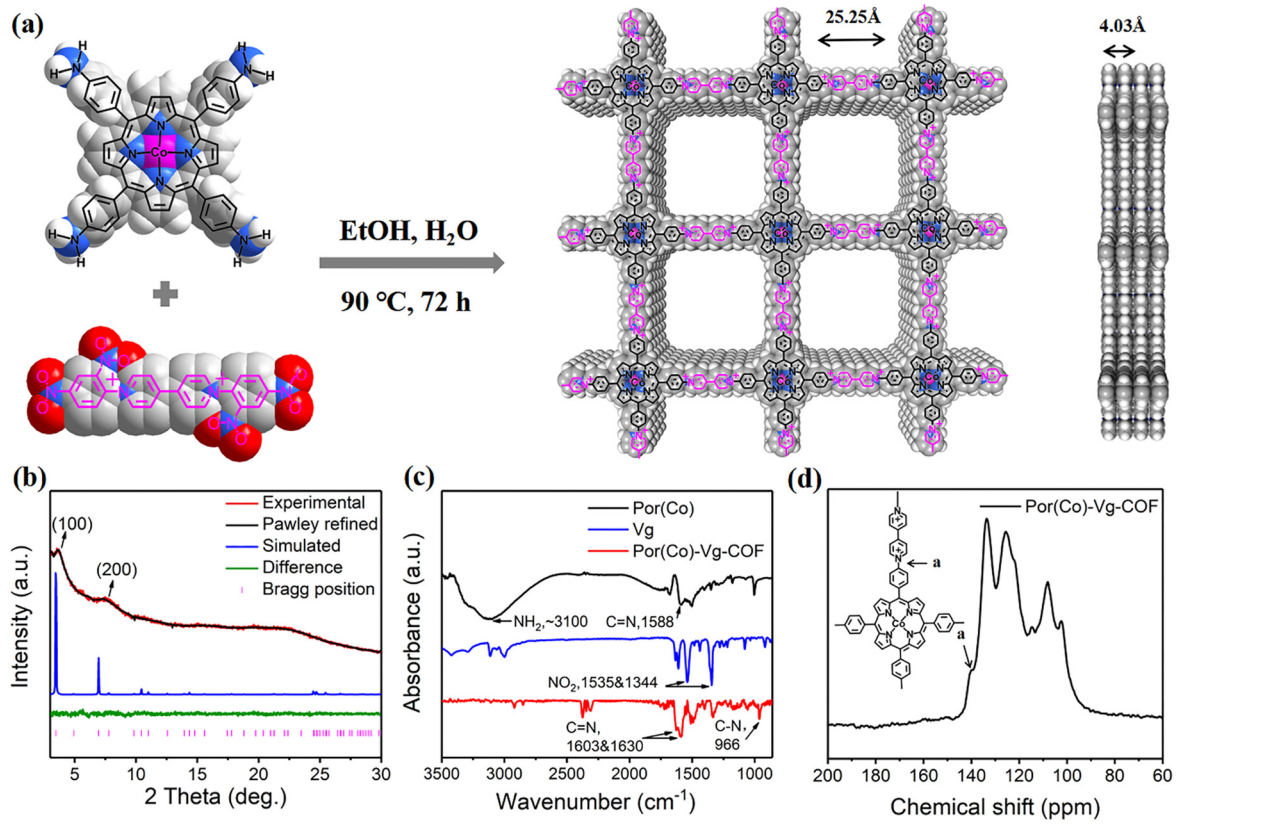

Fig. 1 (a) Illustration of the preparation of Por(Co)-Vg-COF and top and side views of their structure with 2 × 2 square grids in an AA-stacking mode. (b) PXRD patterns of Por(Co)-Vg-COF. (c) FT-IR spectra of Por(Co) (black curve), Por(Co)-Vg-COF (red curve), and Vg (blue curve). (d) Solid-state ^{13}C NMR spectrum of Por(Co)-Vg-COF.

partial current density reached −82 mA cm^{-2} at −1.5 V in 0.06 M H_2SO_4 with 0.5 M K_2SO_4 addictive. More impressively, the Por(Co)-Vg-COF achieved a nearly 100% FE_{CO} over a wide potential range from −0.3 V to −1.2 V and achieved an industrial CO current density of up to 251 mA cm^{-2} in a flow cell in 1 M KOH electrolyte.

Results and discussion

The conjugated 2D COF Por(Co)-Vg-COF was prepared by the solvothermal Zincke reaction of 1,1′-bis(2,4-dinitrophenyl)-[4,4′-bipyridine]-1,1′-dium dichloride (TNV) and 5,10,15,20-tetrakis(4-aminophenyl)porphinatocobalt (Co-TAPP) in a 1 : 2 molar ratio in a mixed solvent of ethanol and water (4 : 1, v : v) for 72 h (Fig. 1(a)). In the process of the Zincke reaction, the Co-TAPP (Por(Co)) and 4-4-bipyridine cationic salt (Vg) building blocks of the Por(Co)-Vg-COF were connected by C–N bonds. Notably, the structure of viologen moieties in Por(Co)-Vg-COF was retained and was quite similar to the methyl viologen (MV) molecules, which can serve as ETMs to provide abundant electrons to the nearby Por(Co) sites. For comparison, the metal-free Por(H)-Vg-COF was also prepared using 5,10,15,20-tetrakis(4-cyanophenyl)porphyrin (TAPP) monomer instead of Por(Co) under similar conditions (Scheme S4, ESI†). To study the role of viologen in Por(Co)-Vg-COF, viologen-free COF-366-Co containing Por(Co) and 1,4-benzenedicarboxaldehyde (BDA) linked by typical imine bonds was also produced by the reported method. It should be noted that although the formation of Por(Co)-Vg-COF was driven by the irreversible Zincke reaction, only weak peaks were observed in the powder X-ray diffraction (PXRD) pattern. Thus, we simulated the Por(Co)-Vg-COF crystal structure using PXRD analysis and Pawley refinements in Materials Studio software. The peaks at the low 2θ angles of 3.70° and 7.46° were assigned to (100) and (200) facets, respectively (Fig. 1(b)), and were in good agreement with the simulated AA-stacking model.[61] The Por(Co)-Vg-COF crystallized in the triclinic *P*1 space group with a unit cell parameter of a = 25.25 Å, b = 25.25 Å, c = 4.03 Å, and α = 90°, β = 90°, γ = 90°. The refinements showed a 1D channel along c-axis with theoretical pore sizes of 2.5 nm, and a distance between adjacent stacked 2D sheets of 4.03 Å. The Fourier-transform infrared (FT-IR) spectrum of Por(Co)-Vg-COF (Fig. 1(c)) showed that the –N–O vibrations bands at 1340 and 1530 cm^{-1} belonging to the TNV and the $-NH_2$ vibrations bands at ∼3100 cm^{-1} attributed to the Por(Co) disappeared after the reaction. Moreover, –C–N– bonds that connected the Por(Co) and Vg stretching vibration band at ∼966 cm^{-1} appeared. In addition, a –C=N– stretching vibration band could be observed at ∼1603 and 1630 cm^{-1}, belonging to the porphyrin and bipyridinium subunits, respectively.[62] The ^{13}C cross-polarization magic angle spinning (CP-MAS) solid-state NMR (Fig. 1(d)) spectrum exhibited a strong peak at 139.91 ppm, corresponding to the pyridyl carbon atoms connecting Por(Co) and Vg. Therefore, these results suggested that Por(Co)-Vg-COF had been successfully synthesized through the Zincke reaction. Por(Co)-Vg-COF was found to have a high Co content of 2.43 wt% by inductively coupled plasma (ICP) optical emission spectrometry (Table S1, ESI†). The CO_2 sorption isotherms showed that the CO_2 uptake value for Por(Co)-Vg-COF was 45 cm^3 g^{-1} (Fig. S5, ESI†), which would be beneficial for promoting the CO_2RR performance.

Scanning electron microscopy (SEM) and transmission electron microscopy (TEM) were used to characterize the morphology of the as-prepared Por(Co)-Vg-COF.[63] The SEM images showed that the Por(Co)-Vg-COF was composed of spherical particles (Fig. S6, ESI†). No aggregated Co or CoO particles were observed in the TEM (Fig. 2(a)) or high-angle annular dark-field scanning transmission electron microscopy (HAADF-STEM) images (Fig. 2(b)). In addition, elemental mapping by energy dispersive X-ray spectroscopy (EDS) showed that the elements C, N, O, Cl, and Co were uniformly distributed in Por(Co)-Vg-COF (Fig. 2(e)). To guarantee the accessibility of the cobalt porphyrin active sites for the electrolytes and CO_2, ultrathin 2D Por(Co)-Vg-COF nanosheets were successfully exfoliated from its bulk *via* high-frequency sonication at room temperature. The atomic force microscopy (AFM) images in Fig. 2(c) and (d) clearly show nanosheets with a thickness of *ca.* 5.5 nm, which was close to thirteen layers of Por(Co)-Vg-COF. Such thin 2D Por(Co)-Vg-COF nanosheets would make the Co active sites highly exposed to the electrolytes and CO_2 in the CO_2RR.

The X-ray photoelectron spectroscopy (XPS) survey spectrum of Por(Co)-Vg-COF (Fig. S7, ESI†) confirmed the presence of C, N, Cl, and Co elements in Por(Co)-Vg-COF, which well matched with the EDS result (Fig. 2(e)). The O resonance peak might have originated from the adsorbed water guest molecules or the residual unreacted nitro groups in the edges of Por(Co)-Vg-COF.

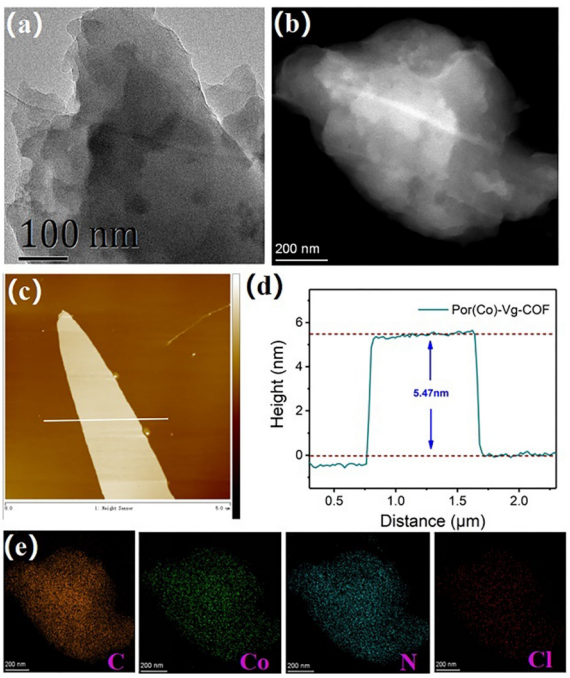

Fig. 2 (a) TEM, (b) HAADF-STEM, and (c) AFM images of Por(Co)-Vg-COF. (d) The height profile along the white line in (c). (e) The elemental mapping of C, Co, N, and Cl for Por(Co)-Vg-COF.

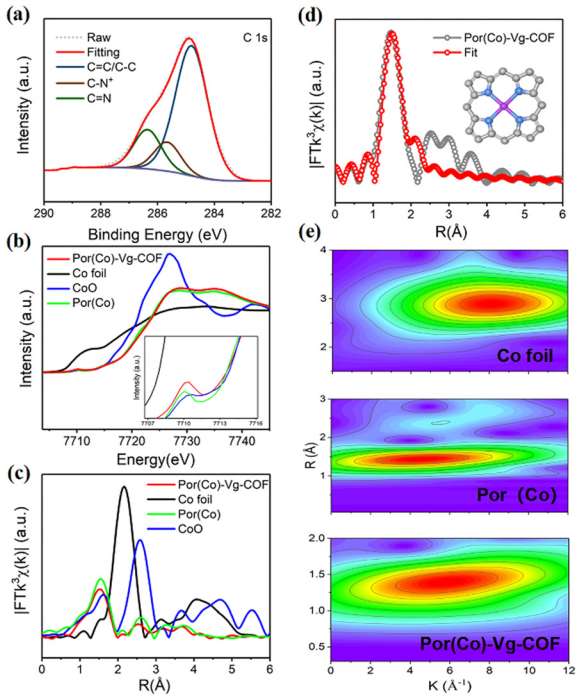

Fig. 3 (a) High-resolution XPS spectra of C 1s for Por(Co)-Vg-COF; (b) Normalized Co K-edge XANES spectra of Por(Co)-Vg-COF, Co foil, CoO, and Por(Co); (c) Fourier-transform EXAFS spectra of Por(Co)-Vg-COF, Co foil, CoO, and Por(Co). (d) EXAFS fitting curves of Por(Co)-Vg-COF (inset: the Ni–N_4 architecture). (e) Wavelet transforms for the k^2-weighted EXAFS signals of different samples.

The C 1s region (Fig. 3(a)) displayed three sets of peaks located at 284.82, 285.6, and 286.4 eV, assignable to C═C/C–C, C–N^+, and C═N, respectively, which proved the viologen in the as-synthesized fresh Por(Co)-Vg-COF was in a dicationic state.[32] The N 1s spectrum (Fig. S8(a), ESI†) of Por(Co)-Vg-COF was fitted with three sets of peaks: cationic pyridinic (398.51 eV), Co-porphyrin (399.13 eV), and N-oxide (401.31 eV), respectively, in which the N–Co bond further verified the Co species was coordinated by N atoms.[64] To investigate the effects of the Vg changes during the electrocatalysis, XPS tests of the Por(Co)-Vg-COF after the CO_2RR were conducted. As shown in Fig. S8(b), ESI,† the N 1s spectrum of Por(Co)-Vg-COF displayed one more peak at 400.9 eV after catalysis, which was ascribed to the neutral pyridinic species, and the Cl 2p spectrum of Por(Co)-Vg-COF disappeared after the catalysis, which proved Vg^+ had changed to Vg^0 during the electrocatalysis (Fig. S9, ESI†). The spectra of the Por(Co)-Vg-COF catalyst before and after the CO_2RR displayed one pair of peaks arising from the spin–orbit doublet of Co 2p (Fig. S10, ESI†), which could be assigned to the Co $2p_{3/2}$ and Co $2p_{1/2}$ with the Co(II) state. The Co $2p_{3/2}$ and Co $2p_{1/2}$ peaks of after catalyst were located at 780.34 and 795.35 eV, which represented an apparent positive shift of ~0.41 eV and ~0.16 eV compared with the pristine Por(Co)-Vg-COF (Co $2p_{3/2}$, 780.75 eV and Co $2p_{1/2}$, 795.51 eV). These changes in binding energies provided direct evidence that the charge-carrier migration pathway might be from Vg to Por(Co).

X-Ray absorption spectroscopy was used to determine the electronic and coordination structures of cobalt in Por(Co)-Vg-COF. The Co K-edge XANES spectra of Por(Co)-Vg-COF showed obvious pre-edge peaks at 7710 eV, which were assigned to a dipole-forbidden 1s → 3d transition (Fig. 3(b)), and a Co K-edge located between those of CoO and Co foil, close to Por(Co), suggesting that the positively charged cobalt in Por(Co)-Vg-COF lay between Co(0) and Co(II).[26] The Co-K edge of the extended X-ray absorption fine structure (EXAFS) appeared as the main signal at 1.50 Å, assigned to the Co–N scattering path (Fig. 3(c)). This was similar to that of Por(Co) (1.47 Å). No obvious signals ascribed to Co–Co (2.17 Å) and Co–O (2.57 Å) were observed, revealing that atomic Co–Nx species predominated and Co or CoO particles were not present in Por(Co)-Vg-COF. In order to determine the Co coordination environment, the EXAFS fitting results were obtained and showed that the coordination number of the Co species within the Por(Co)-Vg-COF was 4.5 (Fig. 3(d) and Table S2, ESI†), suggesting that the Co porphyrin structure was retained after the Zincke reaction. The EXAFS wavelet transform (WT) was further analyzed based on the radial distance resolution and *k*-space resolution to discriminate the backscattering atoms in *R*-space. An intensity maximum attributed to the Co–Co bond was observed in the EXAFS WT contour plots of the Co foil (Fig. 3(e)). While one intensity maximum was observed in the Por(Co) standard sample, which could be ascribed to the Co–N bond. Notably, only one intensity maximum at 5.7 $Å^{-1}$ was observed, which was attributed to Co–N bonding, and no intensity maximum corresponding to Co–Co bonding was present in Por(Co)-Vg-COF, further demonstrating that atomic Co–Nx species predominated and Co particles were not rendered in Por(Co)-Vg-COF.[65]

To further prove the Vg^0 state of the viologen moiety in Por(Co)-Vg-COF had been created during electrocatalysis, the electrochemical behaviour of the Por(Co)-Vg-COF electrode was evaluated by cyclic voltammetry (CV) measurements in 0.2 M Na_2SO_4 aqueous electrolyte.[66] As shown by the CV curves in Fig. S11a, ESI,† two pairs of redox peaks were observed in Por(Co)-Vg-COF, which corresponded to the two-electron redox reaction of the viologen moieties (Fig. S11b, ESI†). Compared with the Vg, a more positive direction shift of the redox potential in Por(Co)-Vg-COF was observed, which may be because the electron-withdrawing group Por(Co) in the framework was more conducive to the redox reaction of Vg. Notably, the redox potential peaks were different from those of the Por(Co) (Fig. S11c, ESI†). So, it is believed that the viologen moieties in Por(Co)-Vg-COF could be reduced to Vg^0 through a two-electron redox reaction under the applied potentials (Scheme S5, ESI†), which was well in accordance with the XPS results. To further reveal the valence change of viologen moieties in Por(Co)-Vg-COF under the negative potentials applied, the UV–vis spectra were recorded in real time during the charging/discharging procedure (Fig. S12, ESI†).[49] During the reduction reaction process of the Por(Co)-Vg-COF electrode, upon the two-electron reduction of the viologen moiety, the absorption band at 411 nm increased proportionally, and in which the position change of the UV absorption peak was consistent with Vg

changing to Vg^0. These further proved Vg^0 of the viologen moiety in Por(Co)-Vg-COF had been produced. Such a change of the viologen moiety from a cationic state to neutral form could improve the electronic conductivity of Por(Co)-Vg-COF, as verified by electrochemical impedance spectroscopy (EIS). As shown in Fig. S13a, ESI,† the semicircle values of Por(Co)-Vg-COF decreased with more negative potentials applied. This indicated that the electron-transfer ability had been significantly enhanced after the Vg^{2+} has changed to Vg^0 in Por(Co)-Vg-COF, which might be ascribed to the formation of the large π conjugation plane including the Vg and Por(Co) parts *via* the C═C bond of Vg^0. In addition, the Por(Co)-Vg-COF displayed a smaller semicircle than the COF-366-Co (Fig. S13b, ESI†). This suggests that the viologen mediator played an important role in the transfer of electrons.

To confirm the charge transfer from the viologen moieties to the electron-acceptor Co-porphyrin in Por(Co)-Vg-COF, differential pulse voltammetry (DPV) tests and solid-state UV spectra measurements of its monomers were conducted.[67] As shown in Fig. S14, ESI,† the first oxidation wave for the Por(Co) was at E^{OX} = 0.91 V and the oxidation wave of the neutral form of Vg was at E^{OX} = −0.37 V. Based on the Tauc plots of the solid-state UV spectra (Fig. S15, ESI†), the band gap (E_g) for Por(Co) was calculated to be 1.84 eV and for Vg^0 was 3.67 eV.[44] The relative positions of the highest occupied molecular orbital and the lowest unoccupied molecular orbital (HOMO–LUMO) were obtained according to the formula: HOMO = $[(eE^{OX} - eE(Fc/Fc^+) + 4.8\ V)]$ eV, and LUMO = HOMO − E_g. The LUMO of Vg with the Vg^0 form possessed a higher potential of −0.31 eV than that of Por(Co) −3.2 eV, which meant it could more easily realize electron transfer from the viologen moieties to Por(Co) (Fig. S16, ESI†). The electrical conductivity in air was measured by the powder particle double electrode method to investigate the superiority of Por(Co)-Vg-COF over COF-366-Co. (Fig. S17 and S18, ESI†).[68] Interestingly, the Por(Co)-Vg-COF had a one order of magnitude higher electron-conduction value (3.7×10^{-7} S m^{-1}) than that of COF-366-Co (2.08×10^{-8} S m^{-1}), which further revealed that the viologen building blocks as ETMs played an important role in promoting the electron transfer and electronic conductivity.

The CO_2RR performances of the Por(Co)-Vg-COF nanosheets were first evaluated in a typical three-electrode system using a gas-tight H-type electrolysis cell with two compartments separated by a proton exchange membrane in 0.5 M $KHCO_3$ aqueous solution.[7] As shown in Fig. 4(a), a more positive onset potential (*ca.* −0.50 V) and significantly higher current densities were obtained in CO_2-saturated electrolyte compared to in the N_2-saturated electrolyte, suggesting a higher CO_2 reactivity than for the HER for the Por(Co)-Vg-COF. To further confirm that the activity was derived from the CO_2RR, the gas and liquid products at different applied potentials from −0.6 to −1.1 V were analyzed by gas chromatography and off-line ^{1}H NMR spectroscopy, respectively. In particular, only CO and H_2 were detected as gaseous products over the entire range of potentials applied, and no liquid product was found in the electrolyte solution (Fig. S19, ESI†). As shown in Fig. 4(b), the

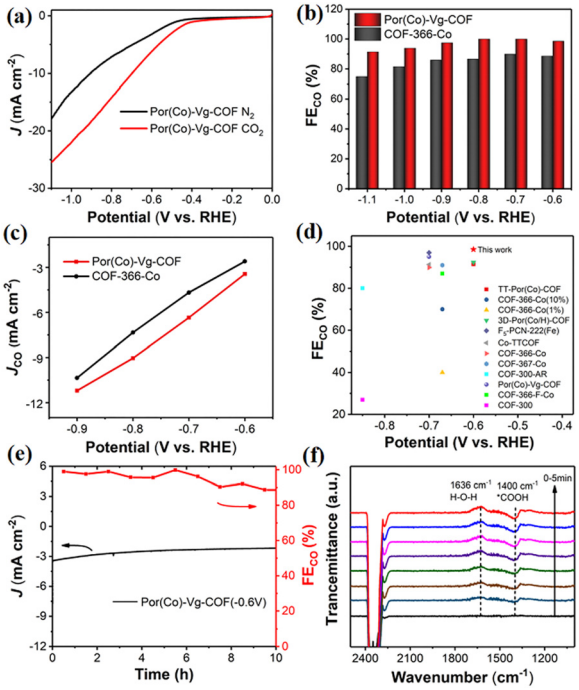

Fig. 4 (a) LSV curves of Por(Co)-Vg-COF in CO_2-saturated and N_2-saturated 0.5 M $KHCO_3$ electrolyte at a scan rate of 10 mV S^{-1}. (b) FE_{CO} from −0.6 to −0.9 V *versus* RHE of Por(Co)-Vg-COF and COF-366-Co. (c) J_{CO} from −0.6 to −0.9 V *versus* RHE of Por(Co)-Vg-COF and COF-366-Co. (d) Comparison of the optimal FE_{CO} among the 2D conductive Por(Co)-Vg-COF and the reported COF electrocatalysts evaluated in a H-type electrochemical cell. (e) Stability test (total current density and FE for CO) at −0.6 V for 10 h. (f) *In situ* ATR-IR of Por(Co)-Vg-COF at −0.9 V.

Por(Co)-Vg-COF exhibited a very high selectivity towards CO production (>98%) in a wide range of the applied potentials of −0.6 V to −1.1 V, which was found to be higher than that of COF-366-Co at the same potential and of other COFs that have been reported (Fig. 4(c), (d) and Table S3, ESI†). In addition, the CO partial current density continuously increased with the increase in potential, reaching −11.2 mA cm^{-2} at −0.9 V, which was higher than for COF-366-Co (Fig. 4(c)). The superior CO_2RR performance for Por(Co)-Vg-COF highlighted the effectiveness of the viologen moiety with the neutral state could as an ETM to deliver electrons fast to Co centres. Moreover, the Por(Co)-Vg-COF displayed long-term stability and the FE_{CO} could retain over 90% after 10 h chronoamperometric test at a fixed potential of −0.6 V in CO_2-saturated 0.5 M $KHCO_3$ solution (Fig. 4(e)). The TEM images (Fig. S20, ESI†) of the Por(Co)-Vg-COF after the CO_2RR revealed that its morphology was unchanged. Furthermore, no significant Co NPs were observed in the TEM images, indicating that the Por(Co) active sites were not reduced to Co(0). XPS analysis (Fig. S21, ESI†) showed no change in the valence state of Co(II) after electrocatalysis. The above results indicated that the Por(Co)-Vg-COF linked by viologen units was a robust framework.

To confirm the active sites of Por(Co)-Vg-COF, we tested the catalytic CO_2RR of Por(H)-Vg-COF without cobalt species under the same conditions. As shown in Fig. S22, ESI,† Por(H)-Vg-COF

showed negligible catalytic activity for the CO_2RR and only the HER happened at various applied potentials. This result indicated that the cobalt centre in Por(Co)-Vg-COF was the active centre for CO_2-to-CO conversion. In addition, the Por(Co)-Vg-COF exhibited a higher FE_{CO} of 98.5% at −0.6 V compared with COF-366-Co without viologen groups. So the efficient electron transfer from viologen to the porphyrin cobalt centre in Por(Co)-Vg-COF promoted the conversion from CO_2 to CO. To confirm that the CO produced was indeed from the reduction of CO_2, ^{13}C isotope labelling experiments were carried out. When $^{13}CO_2$ was used as a substrate, ^{13}CO (m/z = 29) was finally detected by means of mass spectrometry, which confirmed that the CO produced came from the reactant CO_2 and not from the decomposition of the catalysts (Fig. S23, ESI†).

Operando electrochemical attenuated total reflection Fourier-transform infrared spectroscopy (ATR-FTIR) measurements were performed at −0.6 V in CO_2-saturated 0.5 M $KHCO_3$ to verify the possible reaction intermediates in the CO_2RR. The band at ~1400 cm^{-1} in the Por(Co)-Vg-COF spectrum was assigned to the C–O stretching of *COOH, as seen in the ATR-IR spectra (Fig. 4(f)). The intensity of this *COOH signal gradually increased with the time taken to respond, reaching a maximum after 120 s and then reaching dynamic equilibrium. Therefore, for the CO_2RR catalyzed by Por(Co)-Vg-COF, we propose that the formation of the *COOH intermediate was the rate-determining step (RDS).[23] This speculation was consistent with the Tafel slope results (Fig. S24, ESI†), where the values of Por(Co)-Vg-COF were greater than the theoretical value of 118 mV dec^{-1}. This suggests that the formation of *COOH from the adsorbed CO_2 *via* a proton-coupled electron-transfer (PCET) process was the RDS.[26]

To meet the requirements for commercial applications, the excellent CO_2RR performance of Por(Co)-Vg-COF in neutral electrolyte encouraged us to further improve its electrocatalytic performance with a large current density using a gas-diffusion electrode (GDE) in acidic media, which could offer an avenue to reduce carbonate formation and eliminate CO_2 crossover, and this was the first COF catalyst reported for CO_2RR in acidic/alkaline conditions.[37,63–78] The CO_2RR of Por(Co)-Vg-COF in 0.06 M H_2SO_4 with a 0.5 M K_2SO_4 additive was first tested. As shown in Fig. 5(a), a more positive onset potential (−0.75 V) and significantly higher current densities were obtained in CO_2-saturated electrolyte compared to COF-366-Co, suggesting a higher CO_2 reactivity than COF-366-Co for the Por(Co)-Vg-COF in acidic electrolyte. As shown in Fig. 5(b), with the increase in potential, the CO partial current density continuously increased and reached −82 mA cm^{-2} at −1.5 V, which was much higher than that of COF-366-Co. Furthermore, the Por(Co)-Vg-COF exhibited a high selectivity towards CO production (>90%) in the range of the applied potentials of −1.3 V to −1.5 V, and a high FE_{CO} of 91% at −1.3 V (Fig. 5(c)). However, the COF-366-Co only had 20% selectivity towards CO production at the same potential. These results indicated the superior CO_2RR performance for Por(Co)-Vg-COF than COF-366-Co in strong acidic electrolyte and proved that the Por(Co)-Vg-COF was stable in acidic conditions. Besides, we also tested the CO_2RR

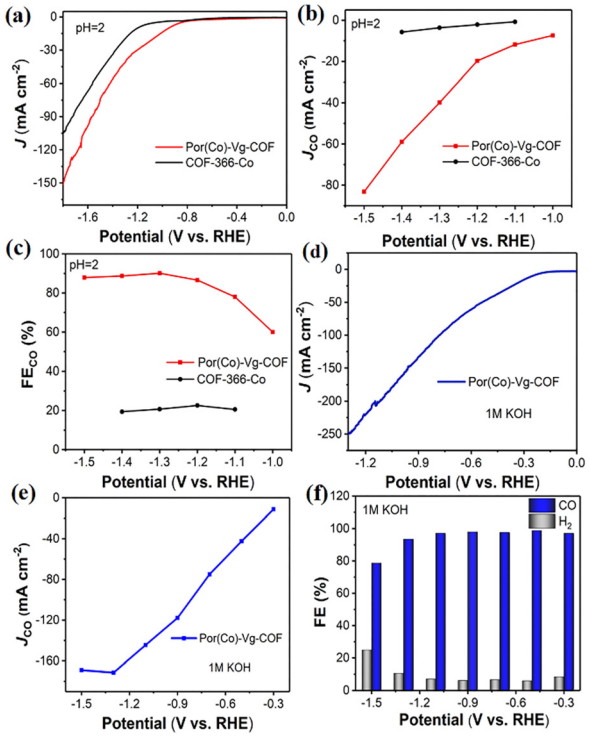

Fig. 5 (a) LSV curves for Por(Co)-Vg-COF and COF-366-Co in 0.06 M H_2SO_4 with a 0.5 M K_2SO_4 additive electrolyte at a scan rate of 10 mV S^{-1}. (b) J_{CO} and (c) FE_{CO} from −1.0 to −1.5 V *versus* RHE of Por(Co)-Vg-COF and COF-366-Co in 0.06 M H_2SO_4 with a 0.5 M K_2SO_4. (d) LSV curves for Por(Co)-Vg-COF in 1 M KOH under CO_2 flow. (e) J_{CO} and (f) FE_{CO} and FE_{H2} from −0.3 to −1.5 V of Por(Co)-Vg-COF in 1 M KOH under CO_2 flow.

performance of Por(Co)-Vg-COF in 1 M KOH aqueous electrolyte. As shown in Fig. 5(d), the total current density reached −251 mA cm^{-2} at −1.3 V and the CO partial current density reached −172 mA cm^{-2} at −1.3 V (Fig. 5(e)). The FE_{CO} was as high as 95% at the wide potential at −0.3 V to −1.2 V (Fig. 5(f)). Compared with the H-cell, the current density of the CO_2RR was significantly improved in the GDE by the faster CO_2 diffusion to the catalyst surface. ICP optical emission spectrometry demonstrated that it had a low Co content of 0.032 mg L^{-1} and 0.0106 mg L^{-1} in acidic and alkaline aqueous electrolytes, respectively (Table S4, ESI†). Moreover, the Por(Co)-Vg-COF displayed long-term stability in 6 h chronoamperometric tests at a fixed potential of −1.3 V in 0.06 M H_2SO_4 with a 0.5 M K_2SO_4 solution and in 9 h chronoamperometric test at a fixed potential of −0.9 V in 1 M KOH solution (Fig. S25 and S26, ESI†). As shown in Fig. S27, ESI,† we obtained the FT-IR spectra of Por(Co)-Vg-COF after soaking in acid and alkali for 4 h respectively, and found that the spectrum did not change. These results suggest that the C–N was more stable in acidic/alkaline aqueous electrolyte and proved the Por(Co)-Vg-COF had excellent CO_2RR performance under harsh conditions.

Conclusions

In summary, strong ETM viologen units were introduced into cobalt porphyrin-based COF (Por(Co)-Vg-COF) through a Zincke

reaction to enhance the electrocatalytic performance of the CO_2RR. As the viologens could undergo a two-electron reduction to achieve an excellent electron-transfer ability, the obtained Por(Co)-Vg-COF nanosheets showed a very high selectivity of 98.5% towards CO production and a large CO partial current density of 9.04 mA cm^{-2} at −0.8 V, which was superior to the insulating COF electrocatalysts. This Por(Co)-Vg-COF material constructed by C–N bond was very stable and is the first COF catalyst reported for the CO_2RR in acidic/alkaline conditions, which could achieve a high FE_{CO} of up to 91% at −1.3 V, and a large CO partial current density up to −82 mA cm^{-2} at −1.5 V in 0.06 M H_2SO_4 with a 0.5 M K_2SO_4 electrolyte. At the same time, the Por(Co)-Vg-COF achieved a nearly 100% FE_{CO} over a wide potential range of −0.3 V to −1.2 V and reached an industrial level CO current density as high as 251 mA cm^{-2} in a flow cell in 1 M KOH electrolyte. This study provides a theoretical basis for the rational design of high-conductivity porous skeleton electrocatalytic materials, as well as an effective strategy for improving the current density and product selectivity of the CO_2RR.

Author contributions

X. Z., H. L., Y. H. and R. C. conceived the project and wrote the manuscript. X. Z., Y. Y., Q. W., H. Z., Y. D. and Q. W. performed the experiments and collected the data. H. L. and Y. H. polished the manuscript. All authors discussed the results and commented on the manuscript.

Conflicts of interest

The authors declare that they have no conflict of interest.

Acknowledgements

This work was financially supported by the National Key Research and Development Program of China (2018YFA0208600, 2018YFA0704502), NSFC (U22A20436, 22071245, 22033008, 22220102005), Fujian Science & Technology Innovation Laboratory for Optoelectronic Information of China (2021ZZ103). We thank the beamline BL14W1 station for XAS measurements at the Shanghai Synchrotron Radiation Facility, China.

Notes and references

1 Q. Wu, M.-J. Mao, Q.-J. Wu, J. Liang, Y.-B. Huang and R. Cao, Construction of Donor–Acceptor Heterojunctions in Covalent Organic Framework for Enhanced CO_2 Electroreduction, *Small*, 2021, **17**, 2004933.

2 H.-J. Zhu, M. Lu, Y.-R. Wang, S.-J. Yao, M. Zhang, Y.-H. Kan, J. Liu, Y. Chen, S.-L. Li and Y.-Q. Lan, Efficient Electron Transmission in Covalent Organic Framework Nanosheets for Highly Active Electrocatalytic Carbon Dioxide Reduction, *Nat. Commun.*, 2020, **11**, 497.

3 Z. B. Zhang, T. Vasiliu, F. F. Li, A. Laaksonen, F. Mocci and X. Y. Ji, Electrochemically Driven Efficient Enzymatic Conversion of CO_2 to Formic Acid with Artificial Cofactors, *J. CO_2* Util., 2021, **52**, 8.

4 Y. H. Zhang, L. Ma, Y. Q. Lv and T. W. Tan, Facile Manufacture of Cof-Based Mixed Matrix Membranes for Efficient CO_2 Separation, *Chem. Eng. J.*, 2022, **430**, 9.

5 X.-D. Zhang, T.-Y. Liu, C. Liu, D.-S. Zheng, J.-M. Huang, Q.-W. Liu, W.-W. Yuan, Y. Yin, L.-R. Huang, M. Xu, Y. Li and Z.-Y. Gu, Asymmetric Low-Frequency Pulsed Strategy Enables Ultralong CO_2 Reduction Stability and Controllable Product Selectivity, *J. Am. Chem. Soc.*, 2023, **145**, 2195–2206.

6 P. H. Zhang, Z. F. Wang, P. Cheng, Y. Chen and Z. J. Zhang, Design and Application of Ionic Covalent Organic Frameworks, *Coord. Chem. Rev.*, 2021, **438**, 15.

7 M.-D. Zhang, D.-H. Si, J.-D. Yi, S.-S. Zhao, Y.-B. Huang and R. Cao, Conductive Phthalocyanine-Based Covalent Organic Framework for Highly Efficient Electroreduction of Carbon Dioxide, *Small*, 2020, **16**, 2005254.

8 Y. Yang, Y. Lu, H.-Y. Zhang, Y. Wang, H.-L. Tang, X.-J. Sun, G. Zhang and F.-M. Zhang, Decoration of Active Sites in Covalent–Organic Framework: An Effective Strategy of Building Efficient Photocatalysis for CO_2 Reduction, *ACS Sustainable Chem. Eng.*, 2021, **9**, 13376–13384.

9 W.-F. Xiong, D.-H. Si, J.-D. Yi, Y.-B. Huang, H.-F. Li and R. Cao, Morphology and Composition Dependence of Multicomponent Cu-Based Nanoreactor for Tandem Electrocatalysis CO_2 Reduction, *Appl. Catal., B*, 2022, **314**, 11.

10 X. Yang, Q.-X. Li, S.-Y. Chi, H.-F. Li, Y.-B. Huang and R. Cao, Hydrophobic Perfluoroalkane Modified Metal-Organic Frameworks for the Enhanced Electrocatalytic Reduction of CO_2, *SmartMat.*, 2022, **3**, 163–172.

11 M.-S. Yang, J.-Q. Sun, Y.-J. Qin, H. Yang, S.-S. Zhang, X.-J. Liu and J. Luo, Hollow Cofe-Layered Double Hydroxide Polyhedrons for Highly Efficient CO_2 Electrolysis, *Sci. China Mater.*, 2022, **65**, 536–542.

12 Q.-Y. Wang, K. Chen, S.-H. Wang, D.-H. Jiang, C.-Q. Ma, L.-X. Zhu and X.-L. Xu, An *in situ*-fabricated p-Co_3O_4@N–ZnO surface heterojunction photocatalyst for solar-to-fuel conversion of CO_2, *Mater. Chem. Front.*, 2023, **7**, 523–534.

13 X.-Q. Wei, Z.-J. Li, H. Jang, M.-G. Kim, Q. Qin and X. Liu, Lattice Strain and Interfacial Engineering of a Bi-Based Electrocatalyst for Highly Selective CO_2 Electroreduction to Formate, *Sci. China Mater.*, 2023, **66**, 1398–1406.

14 D. Wang, Z.-N. Chen, Q.-R. Ding, C.-C. Feng, S.-T. Wang, W. Zhuang and L. Zhang, Rational Preparation of Atomically Precise Non-Alkyl Tin-Oxo Clusters with Theoretical to Experimental Insights into Electrocatalytic CO_2 Reduction Applications, *CCS Chem.*, 2021, **3**, 250–259.

15 F.-L. Ren, W.-J. Hu, C. Wang, P. Wang, W. Li, C.-P. Wu, Y.-F. Yao, W.-J. Luo and Z.-G. Zou, An Extrinsic faradaic Layer on CuSn for High-Performance Electrocatalytic CO_2 Reduction, *CCS Chem.*, 2022, **4**, 1610–1618.

16 J. Liang, Y.-Q. Xie, X.-S. Wang, Q. Wang, T.-T. Liu, Y.-B. Huang and R. Cao, An Imidazolium-Functionalized Mesoporous Cationic Metal-Organic Framework for Cooperative CO_2 Fixation into Cyclic Carbonate, *Chem. Commun.*, 2018, **54**, 342–345.

17 X. Liang, Y. Tian, Y. Yuan and Y. Kim, Ionic Covalent Organic Frameworks for Energy Devices, *Adv. Mater.*, 2021, **33**, e2105647.
18 L.-L. Ling, L. Jiao, X.-S. Liu, Y. Dong, W.-J. Yang, H.-J. Zhang, B.-J. Ye, J. Chen and H.-L. Jiang, Potassium-Assisted Fabrication of Intrinsic Defects in Porous Carbons for Electrocatalytic CO_2 Reduction, *Adv. Mater.*, 2022, **34**, 2205933.
19 Z. Chen, K. Wang, Y.-M. Tang, L. Li, X. Hu, M.-X. Han, Z.-Y. Guo, H.-B. Zhan and B.-L. Chen, Reticular Synthesis of One-Dimensional Covalent Organic Frameworks with 4-C Sql Topology for Enhanced Fluorescence Emission, *Angew. Chem., Int. Ed.*, 2023, **62**, e202213268.
20 Y.-R. Wang, H.-M. Ding, S.-N. Sun, J.-W. Shi, Y.-L. Yang, Q. Li, Y. Chen, S.-L. Li and Y.-Q. Lan, Light, Heat and Electricity Integrated Energy Conversion System: Photothermal-Assisted Co-Electrolysis of CO_2 and Methanol, *Angew. Chem., Int. Ed.*, 2022, **61**, e202212162.
21 X. Yang, J.-Q. Yi, T. Wang, Y.-N. Feng, J.-W. Wang, J. Yu, F.-L. Zhang, Z. Jiang, Z.-S. Lv, H.-C. Li, T. Huang, D.-H. Si, X. Wang, R. Cao and X.-D. Chen, Wet-Adhesive on-Skin Sensors Based on Metal–Organic Frameworks for Wireless Monitoring of Metabolites in Sweat, *Adv. Mater.*, 2022, **34**, 2201768.
22 Y.-Z. Wang, T. Sun, H. B. Mostaghimi Amir, J. Goncalves Tiago, Z.-Z. Liang, Y.-Y. Zhou, W. Zhang, Z.-H. Huang, Y.-H. Ma and R. Cao, Two-Dimensional Metal-Organic Frameworks with Unique Oriented Layers for Oxygen Reduction Reaction: Tailoring the Activity through Exposed Crystal Facets, *CCS Chem.*, 2022, **4**, 1633–1642.
23 S.-Y. Chi, Q. Chen, S.-S. Zhao, D.-H. Si, Q.-J. Wu, Y.-B. Huang and R. Cao, Three-Dimensional Porphyrinic Covalent Organic Frameworks for Highly Efficient Electroreduction of Carbon Dioxide, *J. Mater. Chem. A*, 2022, **10**, 4653–4659.
24 S. Lin, C.-S. Diercks, Y.-B. Zhang, N. Kornienko, E.-M. Nichols, Y.-B. Zhao, A. R. Paris, D. Kim, P. Yang, O. M. Yaghi and C.-J. Chang, Covalent Organic Frameworks Comprising Cobalt Porphyrins for Catalytic CO_2 Reduction in Water, *Science*, 2015, **349**, 1208–1213.
25 A. Mal, S. Vijayakumar, R. K. Mishra, J. Jacob, R. S. Pillai, B. S. Dileep Kumar and A. Ajayaghosh., Supramolecular Surface Charge Regulation in Ionic Covalent Organic Nanosheets: Reversible Exfoliation and Controlled Bacterial Growth, *Angew. Chem., Int. Ed.*, 2019, **59**, 8713–8719.
26 Q.-J. Wu, D.-H. Si, Q. Wu, Y.-L. Dong, R. Cao and Y.-B. Huang, Boosting Electroreduction of CO_2 over Cationic Covalent Organic Frameworks: Hydrogen Bonding Effects of Halogen Ions, *Angew. Chem., Int. Ed.*, 2023, **62**, e202215687.
27 Q. Wu, R.-K. Xie, M.-J. Mao, G.-L. Chai, J.-D. Yi, S.-S. Zhao, Y.-B. Huang and R. Cao, Integration of Strong Electron Transporter Tetrathiafulvalene into Metalloporphyrin-Based Covalent Organic Framework for Highly Efficient Electroreduction of CO_2, *ACS Energy Lett.*, 2020, **5**, 1005–1012.
28 Y. Li, J.-F. Sui, L.-S. Cui and H.-L. Jiang, Hydrogen Bonding Regulated Flexibility and Disorder in Hydrazone-Linked Covalent Organic Frameworks, *J. Am. Chem. Soc.*, 2023, **145**, 1359–1366.
29 S. Dou, J. Song, S. Xi, Y. Du, J. Wang, Z.-F. Huang, Z. J. Xu and X. Wang, Boosting Electrochemical CO_2 Reduction on Metal–Organic Frameworks *via* Ligand Doping, *Angew. Chem., Int. Ed.*, 2019, **58**, 4041–4045.
30 H. Xiao, H. Zhu, W. Weng, K. Li, W. Li and W. Xiao, Electrochemical fixation of CO_2 over a Mo plate to prepare a Mo_2C film for electrocatalytic hydrogen evolution, *Mater. Chem. Front.*, 2021, **5**, 4963–4969.
31 F. Lü, H. Bao, F. He, G. Qi, J. Sun, S. Zhang, L. Zhuo, H. Yang, G. Hu, J. Luo and X. Liu, Nitrogen dopant induced highly selective CO_2 reduction over lotus-leaf shaped ZnO nanorods, *Mater. Chem. Front.*, 2021, **5**, 4225–4230.
32 W.-Q. Li, Z.-Y. Zhao, W.-B. Hu, Q.-Q. Cheng, L.-J. Yang, Z. Hu, Y. A. Liu, K. Wen and H. Yang, Design of Thiazolo[5,4-*D*]Thiazole-Bridged Ionic Covalent Organic Polymer for Highly Selective Oxygen Reduction to H_2O_2, *Chem. Mater.*, 2020, **32**, 8553–8560.
33 J. Szczesny, A. Ruff, A. R. Oliveira, M. Pita, I. A. C. Pereira, A. L. De Lacey and W. Schuhmann., Electroenzymatic CO_2 Fixation Using Redox Polymer/Enzyme-Modified Gas Diffusion Electrodes, *ACS Energy Lett.*, 2020, **5**, 321–327.
34 Y. Qiao, W.-C. Lai, K. Huang, T.-T. Yu, Q.-Y. Wang, L. Gao, Z.-L. Yang, Z.-S. Ma, T.-L. Sun, M. Liu, C. Lian and H.-W. Huang, Engineering the Local Microenvironment over Bi Nanosheets for Highly Selective Electrocatalytic Conversion of CO_2 to HCOOH in Strong Acid, *ACS Catal.*, 2022, **12**, 2357–2364.
35 J. E. Huang, F.-W. Li, A. Ozden, A. Sedighian Rasouli, F. P. García de Arquer, S.-J. Liu, S.-Z. Zhang, M.-C. Luo, X. Wang, Y.-W. Lum, Y. Xu, K. Bertens, R.-K. Miao, C.-T. Dinh, D. Sinton and E. H. Sargent, CO_2 Electrolysis to Multicarbon Products in Strong Acid, *Science*, 2021, **372**, 1074–1078.
36 A. Goyal, G. Marcandalli, V. A. Mints and M. T. M. Koper, Competition between CO_2 Reduction and Hydrogen Evolution on a Gold Electrode under Well-Defined Mass Transport Conditions, *J. Am. Chem. Soc.*, 2020, **142**, 4154–4161.
37 J. Lee, J. Lim, C.-W. Roh, H. S. Whang and H. Lee, Electrochemical CO_2 Reduction Using Alkaline Membrane Electrode Assembly on Various Metal Electrodes, *J. CO_2* Util., 2019, **31**, 244–250.
38 H.-F. Li, T.-F. Liu, P.-F. Wei, L. Lin, D.-F. Gao, G.-X. Wang and X. Bao, High-Rate CO_2 Electroreduction to C_{2+} Products over a Copper-Copper Iodide Catalyst, *Angew. Chem., Int. Ed.*, 2021, **60**, 14329–14333.
39 J. Li, Z.-Y. Wang, C. McCallum, Y. Xu, F.-W. Li, Y.-H. Wang, C. M. Gabardo, D. Cao-Thang, T.-T. Zhuang, L. Wang, J. Y. Howe, Y. Ren, E. H. Sargent and D. Sinton, Constraining Co Coverage on Copper Promotes High-Efficiency Ethylene Electroproduction, *Nat. Catal.*, 2019, **2**, 1124–1131.
40 R.-R. Li, F. Liu, Y.-H. Zhang, M.-M. Guo and D. Liu, Nitrogen, Sulfur Co-Doped Hierarchically Porous Carbon as a Metal-Free Electrocatalyst for Oxygen Reduction and Carbon Dioxide Reduction Reaction, *ACS Appl. Mater. Interfaces*, 2020, **12**, 44578–44587.

41 T. Moeller, W. Ju, A. Bagger, X.-L. Wang, F. Luo, T. Trung Ngo, A. S. Varela, J. Rossmeisl and P. Strasser, Efficient CO_2 to CO Electrolysis on Solid Ni-N-C Catalysts at Industrial Current Densities, *Energy Environ. Sci.*, 2019, **12**, 640–647.
42 M. C. O. Monteiro, F. Dattila, N. Lopez and M. T. M. Koper, The Role of Cation Acidity on the Competition between Hydrogen Evolution and CO_2 Reduction on Gold Electrodes, *J. Am. Chem. Soc.*, 2022, **144**, 1589–1602.
43 C. P. O'Brien, R.-K. Miao, S.-J. Liu, Y. Xu, G. Lee, A. Robb, J. E. Huang, K. Xie, K. Bertens, C. M. Gabardo, J. P. Edwards, C.-T. Dinh, E. H. Sargent and D. Sinton, Single Pass CO_2 Conversion Exceeding 85% in the Electrosynthesis of Multicarbon Products *Via* Local CO_2 Regeneration, *ACS Energy Lett.*, 2021, **6**, 2952–2959.
44 Y. Wang, M.-Y. Wang, Z.-S. Zhang, Q. Wang, Z. Jiang, M. Lucero, X. Zhang, X.-X. Li, M. Gu, Z.-X. Feng and Y.-Y. Liang, Phthalocyanine Precursors to Construct Atomically Dispersed Iron Electrocatalysts, *ACS Catal.*, 2019, **9**, 6252–6261.
45 Z.-L. Yin, H.-Q. Peng, X. Wei, H. Zhou, J. Gong, M.-M. Huai, L. Xiao, G.-W. Wang, J.-T. Lu and L. Zhuang, An Alkaline Polymer Electrolyte CO_2 Electrolyzer Operated with Pure Water, *Energy Environ. Sci.*, 2019, **12**, 8.
46 W. Shin, S. Lee, J. Shin, S. Lee and Y. Kim, Highly Selective Electrocatalytic Conversion of CO_2 to CO at −0.57 V (NHE) by Carbon Monoxide Dehydrogenase from Moorella Thermoacetica, *J. Am. Chem. Soc.*, 2003, **125**, 14688–14689.
47 B. C. De Simone, T. Marino and N. Russo, TDDFT Investigation on Methylviologen, 3,7-Diazabenzophosphole, and Helical Helquat Electrochromic Systems, *Theor. Chem. Acc.*, 2016, **135**, 9.
48 J.-J. Ding, C.-N. Zheng, L.-X. Wang, C.-B. Lu, B. Zhang, Y. Chen, M.-Q. Li, G.-Q. Zhai and X.-D. Zhuang, Viologen-Inspired Functional Materials: Synthetic Strategies and Applications, *J. Mater. Chem. A*, 2019, **7**, 23337–23360.
49 Z. Wang, X. Jia, P. Zhang, Y. Liu, H. Qi, P. Zhang, U. Kaiser, S. Reineke, R. Dong and X. Feng, Viologen-Immobilized 2D Polymer Film Enabling Highly Efficient Electrochromic Device for Solar-Powered Smart Window, *Adv. Mater.*, 2021, **34**, 9.
50 V. Fourmond and C. Leger, Dinitrogen Reduction: Interfacing the Enzyme Nitrogenase with Electrodes, *Angew. Chem., Int. Ed.*, 2017, **56**, 4388–4390.
51 H. Noh, C.-W. Kung, K.-I. Otake, A. W. Peters, Z.-Y. Li, Y.-J. Liao, X.-Y. Gong, O. K. Farha and J. T. Hupp., Redox-Mediator-Assisted Electrocatalytic Hydrogen Evolution from Water by a Molybdenum Sulfide-Functionalized Metal-Organic Framework, *ACS Catal.*, 2018, **8**, 9848–9858.
52 L. Chen, C. Lin and R. G. Compton, Single Entity Electrocatalysis: Oxygen Reduction Mediated *Via* Methyl Viologen Doped Nafion Nanoparticles, *Phys. Chem. Chem. Phys.*, 2018, **20**, 15795–15806.
53 T. Skorjanc, D. Shetty, F. Gandara, L. Ali, J. Raya, G. Das, M. A. Olson and A. Trabolsi, Remarkably Efficient Removal of Toxic Bromate from Drinking Water with a Porphyrin–Viologen Covalent Organic Framework, *Chem. Sci.*, 2020, **11**, 845–850.
54 G. Das, T. Skorjanc, S. K. Sharma, F. Gandara, M. Lusi, D. S. Shankar Rao, S. Vimala, S. Krishna Prasad, J. Raya, D. S. Han, R. Jagannathan, J. C. Olsen and A. Trabolsi, Viologen-Based Conjugated Covalent Organic Networks *Via* Zincke Reaction, *J. Am. Chem. Soc.*, 2017, **139**, 9558–9565.
55 L. Liu, Q. Liu, R. Li, M.-S. Wang and G.-C. Guo, Controlled Photoinduced Generation of "Visual" Partially and Fully Charge Separated States in Viologen Analogues, *J. Am. Chem. Soc.*, 2021, **143**, 2232–2238.
56 G. A. Leith, C. R. Martin, A. Mathur, P. Kittikhunnatham, K. C. Park and N. B. Shustova, Dynamically Controlled Electronic Behavior of Stimuli-Responsive Materials: Exploring Dimensionality and Connectivity, *Adv. Energy Mater.*, 2021, **12**, 23.
57 T. Komura, T. Yamaguchi, K. Furuta and K. Sirono, Irreversible Transformation of Polypyrrole-Bound Viologen with Two-Electron Reduction in Acidic Aqueous Solutions, *J. Electroanal. Chem.*, 2002, **534**, 123–130.
58 X. Li, S. Xi, L. Sun, S. Dou, Z. Huang, T. Su and X. Wang, Isolated FeN_4 Sites for Efficient Electrocatalytic CO_2 Reduction, *Adv. Sci.*, 2020, **7**, 2001545.
59 L. Sun, Z. Huang, V. Reddu, T. Su, A. C. Fisher and X. Wang, A Planar, Conjugated N_4-Macrocyclic Cobalt Complex for Heterogeneous Electrocatalytic CO_2 Reduction with High Activity, *Angew. Chem., Int. Ed.*, 2020, **59**, 17104–17109.
60 J. Wang, X. Huang, S. Xi, J.-M. Lee, C. Wang, Y. Du and X. Wang, Linkage Effect in the Heterogenization of Cobalt Complexes by Doped Graphene for Electrocatalytic CO_2 Reduction, *Angew. Chem., Int. Ed.*, 2019, **58**, 13532–13539.
61 N. Li, D.-H. Si, Q.-J. Wu, Q. Wu, Y.-B. Huang and R. Cao, Boosting Electrocatalytic CO_2 Reduction with Conjugated Bimetallic Co/Zn Polyphthalocyanine Frameworks, *CCS Chem.*, 2022, 1–14.
62 T. Skorjanc, D. Shetty, F. Gándara, L. Ali, J. Raya, G. Das, M. A. Olson and A. Trabolsi, Remarkably Efficient Removal of Toxic Bromate from Drinking Water with a Porphyrin-Viologen Covalent Organic Framework, *Chem. Sci.*, 2020, **11**, 845–850.
63 C. Liu, X.-D. Zhang, J.-M. Huang, M.-X. Guan, M. Xu and Z.-Y. Gu, *In Situ* Reconstruction of Cu–N Coordinated MOFs to Generate Dispersive Cu/Cu_2O Nanoclusters for Selective Electroreduction of CO_2 to C_2H_4, *ACS Catal.*, 2022, **12**, 15230–15240.
64 Q.-X. Li, D.-H. Si, W. Lin, Y.-B. Wang, H.-J. Zhu, Y.-B. Huang and R. Cao, Highly Efficient Electroreduction of CO_2 by Defect Single-Atomic Ni–N-3 Sites Anchored on Ordered Micro-Macroporous Carbons, *Sci. China: Chem.*, 2022, **65**, 1584–1593.
65 J.-D. Yi, D.-H. Si, R. Xie, Q. Yin, M.-D. Zhang, Q. Wu, G.-L. Chai, Y.-B. Huang and R. Cao, Conductive Two-Dimensional Phthalocyanine-Based Metal–Organic Framework Nanosheets for Efficient Electroreduction of CO_2, *Angew. Chem., Int. Ed.*, 2021, **60**, 17108–17114.
66 L. Chen, H. Willcock, C.-J. Wedge, F. Hartl, H.-M. Colquhoun and B.-W. Greenland, Efficient Access to Conjugated 4,4′-Bipyridinium Oligomers Using the Zincke

Reaction: Synthesis, Spectroscopic and Electrochemical Properties, *Org. Biomol. Chem.*, 2016, **14**, 980–988.

67 K. Qian, X. Guan, N. Sun and H.-L. Jiang, Precise Fabrication of Ternary Ordered Covalent Organic Frameworks for Photocatalysis, *Sci. China: Chem.*, 2023, **66**, 436–442.

68 N. Keller, M. Calik, D. Sharapa, H. R. Soni, P. M. Zehetmaier, S. Rager, F. Auras, A. C. Jakowetz, A. Görling, T. Clark and T. Bein, Enforcing Extended Porphyrin J-Aggregate Stacking in Covalent Organic Frameworks, *J. Am. Chem. Soc.*, 2018, **140**, 16544–16552.

69 L. Sun, S. S. Park, D. Sheberla and M. Dincă, Measuring and Reporting Electrical Conductivity in Metal–Organic Frameworks: Cd_2(TTFTB) as a Case Study, *J. Am. Chem. Soc.*, 2016, **138**, 14772–14782.

70 H. Zhao, H. Cao, Z. Zhang and Y.-G. Wang, Modeling the Potential-Dependent Kinetics of CO_2 Electroreduction on Single-Nickel Atom Catalysts with Explicit Solvation, *ACS Catal.*, 2022, **12**, 11380–11390.

71 Y. Wu, Q. Chen, J. Zhu, K. Zheng, M. Wu, M. Fan, W. Yan, J. Hu, J. Zhu, Y. Pan, X. Jiao, Y. Sun and Y. Xie, Selective CO_2-to-C_2H_4 Photoconversion Enabled by Oxygen-Mediated Triatomic Sites in Partially Oxidized Bimetallic Sulfide, *Angew. Chem., Int. Ed.*, 2023, **62**, e202301075.

72 Y. Li, J. Sui, L.-S. Cui and H.-L. Jiang, Hydrogen Bonding Regulated Flexibility and Disorder in Hydrazone-Linked Covalent Organic Frameworks, *J. Am. Chem. Soc.*, 2023, **145**, 1359–1366.

73 B. Sheng, D. Cao, H. Shou, W. Xu, C. Wu, P. Zhang, C. Liu, Y. Xia, X. Wu, S. Chu, J. Zhang, L. Song and S. Chen, Anomalous Ru Dissolution Enabling Efficient Integrated CO_2 Electroreduction in Strong Acid, *Chem. Eng. J.*, 2023, **454**, 9.

74 Z. Jiang, Z. S. Zhang, H. Li, Y. R. Tang, Y. B. Yuan, J. Zao, H. Z. Zheng and Y. Y. Liang, Molecular Catalyst with near 100% Selectivity for CO_2 Reduction in Acidic Electrolytes, *Adv. Energy Mater.*, 2023, **13**, 2203603.

75 J.-C. Hu, J. Wu, B.-Y. Deng and F. Wang, An assembled ternary photocatalyst CoPh/CdSe@TiO_2 for simultaneous photocatalytic CO_2 and proton reduction, *Mater. Chem. Front.*, 2023, **7**, 514–522.

76 Y. Li, M. Karimi, Y. N. Gong, N. Dai, V. Safarifard and H. L. Jiang, Integration of Metal-Organic Frameworks and Covalent Organic Frameworks: Design, Synthesis, and Applications, *Matter*, 2021, **4**, 2230–2265.

77 Y. Duan, X.-L. Zhang, F.-Y. Gao, Y. Kong, Y. Duan, X.-T. Yang, X.-X. Yu, Y.-R. Wang, S. Qin, Z. Chen, R. Wu, P.-P. Yang, X.-S. Zheng, J.-F. Zhu, M.-R. Gao, T.-B. Lu, Z.-Y. Yu and S.-H. Yu, Interfacial Engineering of Ni/V_2O_3 Heterostructure Catalyst for Boosting Hydrogen Oxidation Reaction in Alkaline Electrolytes, *Angew. Chem., Int. Ed.*, 2023, **62**, e202217275.

78 M.-D. Zhang, J.-D. Yi, Y.-B. Huang and R. Cao, Covalent Triazine Frameworks-Derived N,P Dual-Doped Porous Carbons for Highly Efficient Electrochemical Reduction of CO_2, *Chin. J. Struct. Chem.*, 2021, **40**, 1213–1222.

